

9-21-2020

Analysis of Local Seismic Events near a Large-N Array for Moho Reflections

Qicheng Zeng

Robert L. Nowack

Follow this and additional works at: <https://docs.lib.purdue.edu/gdstr>

This document has been made available through Purdue e-Pubs, a service of the Purdue University Libraries.
Please contact epubs@purdue.edu for additional information.

8 **Abstract**

9 Local seismic events recorded by the large-N IRIS Community Wavefield Experiment in
10 Oklahoma are used to estimate Moho reflections near the array. For events within 50 km of the
11 center of the array, normal moveout corrections and receiver stacking are applied to identify the
12 *PmP* and *SmS* Moho reflections on the vertical and transverse components. Corrections for the
13 reported focal depths are applied to a uniform event depth. To stack signals from multiple events,
14 further static corrections of the envelopes of the Moho reflected arrivals from the individual event
15 stacks are applied. The multiple-event stacks are then used to estimate the pre-critical *PmP* and
16 *SmS* arrivals, and an average Poisson's ratio of 1.77 ± 0.02 was found for the crust near the array.
17 Using a modified Oklahoma Geological Survey (OGS) velocity model with this Poisson's ratio,
18 the time-to-depth converted *PmP* and *SmS* arrivals resulted in a Moho depth of 41 ± 6 km. The
19 modeling of wide-angle Moho reflections for selected events at epicenter-to-station distances of
20 90 to 135 km provides additional constraints, and assuming the modified OGS model, a Moho
21 depth of 40 ± 1 km was inferred. The difference between the pre-critical and wide-angle Moho
22 estimates could result from some lateral variability between the array and the wide-angle events.
23 However, both estimates are slightly shallower than the original OGS model Moho depth of 42
24 km, and this could also result from a somewhat faster lower crust. This study shows that local
25 seismic events, including induced events, can be utilized to estimate properties and structure of the
26 crust, which in turn can be used to better understand the tectonics of a given region. The recording
27 of local seismicity on large-N arrays provides increased lateral phase coherence for the better

28 identification of pre-critical and wide-angle reflected arrivals.

29 **Keywords:** Large-N seismic arrays, Moho reflections, Crustal Poisson's ratio

30 **Introduction**

31 New advances in seismic instrumentations have made it possible to deploy arrays with a large
32 number of seismometers (large-N arrays). The seismic sensors used in these large-N experiments
33 are small, inexpensive systems which allow for fast deployments, and incorporate a geophone, a
34 data logger, a GPS clock, and power (Freed, 2008; Karplus and Schmandt, 2018; Ringler et al.,
35 2018). Some of the first academic applications of large-N arrays used single-component seismic
36 nodes, including experiments conducted near Long Beach, California (Lin et al., 2013; Schmandt
37 and Clayton, 2013; Nakata et al., 2015; Riahi and Gerstoft, 2015; Z. Li et al., 2018), Mount Saint
38 Helens (Hansen and Schmandt, 2015; Hansen et al., 2016; Kiser et al., 2016, 2019; Wang et al.,
39 2017; Glasgow et al., 2018), and along the San Jacinto fault zone (Hillers et al., 2016; Roux et al.,
40 2016). Recent seismic studies involving three-component nodes have also demonstrated the wide
41 application of large-N arrays for the fault zones (Qin et al., 2018; Wang et al., 2019), geothermal
42 areas (Brenquier et al., 2016; Ward and Lin, 2017; Wu et al., 2017), for earthquake mechanism
43 studies (Fan and McGuire, 2018), and for the analysis of cultural signals (C. Li et al., 2018).

44 A number of array based approaches have been used to study seismic body waves from the
45 Moho, including controlled-source wide-angle reflection and refraction methods (e.g. Cook et al.,
46 2010; Prodehl and Mooney, 2012; Carbonell et al., 2013). The *PmP* and *SmS* phases from
47 earthquake sources have also been recorded on dense arrays being used for active-source studies,
48 for example by Mechie et al. (2012) for determining crustal *S*-velocities and Poisson's ratio along

49 the INDEPTH IV profile in northeast Tibet. Mori and Helmberger (1996) used closely spaced
50 aftershocks from the 1992 Landers earthquake in southern California to observe *SmS* Moho
51 reflections. Wang et al. (2018) used measurements of *P* and *PmP* arrivals from aftershocks and
52 local earthquakes to perform crustal tomography in western Japan. Griffin et al. (2011)
53 investigated the velocity structure of the Tibetan Lithosphere using travel-times from *P* and *PmP*
54 arrivals from regional earthquakes recorded on the large-scale Hi-CLIMB array.

55 Array based methods have also been applied for seismic receiver functions from teleseismic
56 earthquakes (e.g. Levander and Nolet, 2005; Rondenay, 2009; Nowack et al., 2010). Virtual deep
57 seismic sounding (VDSS) using the *SsPmp* phases has been used for array based imaging of the
58 crust and Moho from earthquake sources (Tseng et al., 2009; Yu et al., 2013; Thompson et al.,
59 2019). Seismic interferometry has also been applied to teleseismic earthquake sources recorded by
60 seismic arrays using global-phase seismic interferometry (Ruigrok and Wapenaar, 2012; Nishitsuji
61 et al., 2016).

62 Shen and Ritzwoller (2016) utilized observations from ambient noise and earthquakes,
63 receiver functions and Rayleigh wave ellipticity using the USArray transportable array to study
64 the crust and upper mantle beneath the continental U.S., including the broader features beneath
65 Oklahoma. Evanzia et al. (2014) conducted V_p and V_s tomography of the crust and upper mantle
66 beneath Texas and Oklahoma, and Zhu (2018) performed tomography of ambient noise for crustal
67 structure of North Texas and Oklahoma. In these studies, features in southern, eastern and
68 southwestern Oklahoma including the Anadarko basin, Wichita uplift, the Arkoma basin and the

69 Ouachita uplift could be observed in the tomographic images.

70 A state-wide velocity model in Oklahoma was developed by Marsh (2018) using ambient
71 noise tomography down to about 20 km in depth, where slower regions were associated with basin
72 structures and faster regions with shallower basement. Ratre and Behm (2019) developed a 3D
73 model of central Oklahoma from the combination of 1D travel-time curves resulting from the
74 stacking and inversion of P_g waveforms. They found a generally homogeneous crust with some
75 velocity variations related to regional geological structures. They also estimated a higher speed
76 lower crust inferring a more mafic lower crust, and used this to assess the extent of the mid-
77 continent rift in Oklahoma. Pei et al (2018) performed P_g tomography with anisotropy to
78 investigate crustal seismogenic features in central Oklahoma and correlated these with recent
79 seismic activity. Wang et al. (2019) applied P-to-S receiver functions from teleseismic earthquakes
80 to investigate the crust of Oklahoma.

81 Inamori et al. (1992) utilized seismic reflection methods to image mid-crustal structure using
82 aftershock waveforms from the 1984 Western Nagano Prefecture earthquake in Japan. Quiros et
83 al. (2007) applied reflection imaging of aftershocks from the Mw 5.8, 2011 Virginia earthquake
84 recorded by several dense seismic arrays to image crustal reflections. Vertical seismic profiling
85 (VSP) was utilized for earthquake events followed by VSP-CRP transformations to account for
86 offset and depth of the events. Eddy and Harder (2018) investigated the correlation of local
87 earthquakes from the IRIS Community Wavefield Experiment in north-central Oklahoma to form
88 a reflection image of reflectors in the basement and sedimentary section.

89 In this study, later arrivals from frequent local seismic events near the IRIS Community
90 Wavefield Experiment in Oklahoma (Anderson, et al., 2016; Sweet et al., 2018) are used to
91 estimate Moho reflections and crustal Poisson's ratio near the array. This is followed by a normal
92 move-out correction and stacking to an equivalent zero offset. Laterally homogeneous velocities
93 and Moho depth in the vicinity of the array are assumed, with static corrections applied to account
94 for small velocity variability and uncertainties in the earthquake locations. Since the event depths
95 are much shallower than the Moho depth, a reflection methodology is applied rather than full VSP
96 processing.

97 Seismic events with locations from the Oklahoma Geological Survey Earthquake catalog
98 (OGS Earthquake Catalog, 2016, Walter, et al., 2020) near the array are utilized. Waveform-
99 relocation and template-matching studies have also been performed by Schoenball and Ellsworth
100 (2017) and Skoumal et al. (2019). Many of the seismic events in Oklahoma are now identified as
101 induced events from oil and gas activities, and in particular from waste water injection (Ellsworth,
102 2013; Keranen et al., 2014; Walsh and Zoback, 2015; Weingarten et al., 2015; Langenbruch and
103 Zoback, 2016; Hincks et al., 2018).

104 We first analyzed the *P*- and *S*-wave later arrivals on the vertical and transverse components
105 for selected events within 50 km from the center of the array. We identified the Moho reflections
106 on the vertical and transverse components for individual events by applying normal moveout
107 corrections and receiver stacking. *P*-wave and *S*-wave Moho reflection signals were enhanced by
108 multiple-event stacking after static corrections and polarity sign corrections were applied. These

109 stacks were then used to infer average crustal V_p/V_s ratio, Poisson's ratio and Moho depth near
110 the array. We also modeled wide-angle PmP and SmS Moho reflections for selected events at
111 epicenter-to-station distances of 90 to 135 km, which provides additional constraints. The analysis
112 of local seismicity, including induced seismicity in areas with less natural seismicity, can be used
113 to estimate the properties and structure of the crust, which in turn can be utilized to better
114 understand the tectonics of a given region. The recording of local seismicity on large-N arrays
115 allows for increased lateral phase coherence for the better identification of smaller seismic arrivals.

116 **Seismic Data**

117 The seismic data used in this study are selected from the Oklahoma Geological Survey (OGS)
118 Earthquake Catalog from June 24 to July 20, 2016 (OGS Earthquake Catalog, 2016). The seismic
119 events were recorded by the seismic stations of IRIS (Incorporated Research Institutions for
120 Seismology) Community Wavefield Experiment in Oklahoma. Fig. 1a) shows the locations of
121 seismic events with epicenters less than 50 km from the center of the array. Selected events in this
122 distance range are then used to investigate P- and S-wave Moho reflections. The seismic array and
123 a 50 km radius region around it, including the selected events, are also shown in Fig. 1b), along
124 with the major geological features in Oklahoma (Johnson, 2008).

125 The IRIS Community Wavefield Experiment included 363 nodal sensors deployed along three
126 lines, a 7-layer gradiometer nodal array, and 18 broadband stations collocated with 9 infrasound
127 stations (Sweet et al., 2018). The nodes deployed in this experiment were Z-Land Fairfield nodal
128 5 Hz three-component sensors with ~35 days of battery life and a 250 samples/s sampling rate.

129 The right inset of Fig. 1a) shows the geometry of the seismometers in the array. The triangles
130 are the north-south and east-west linear nodal array stations, the diamonds denote stations from
131 the nodal gradiometer array. The spacing between the nodes along the north-south and east-west
132 lines was about 100 m. The length of the east-west line is about 13 km, and the length of the north-
133 source lines are about 5 km. The linear array nodal sensors were deployed from 20 June to July
134 20 for about 30 days (Sweet et al., 2018). The squares are the 18 broadband stations, which were
135 deployed from June 20 to November 10, 2016 for about five months. For this study, the east-west
136 linear nodal array stations were utilized to analyze the seismic events near the array.

137 A reference velocity model for Oklahoma from the Oklahoma Geological Survey (Darold et
138 al., 2015) is shown in Figure 2 and is denoted by solid lines, with the S-wave velocities on the left
139 and P-wave velocities on the right. The OGS velocity model assumes a constant 1.73 V_p/V_s ratio.
140 A modified S-velocity model with a V_p/V_s ratio of 1.77 obtained from the analysis of *PmP* and
141 *SmS* arrivals in this study is also shown in Figure 2 denoted by the dashed line. For comparison,
142 the velocity model for locations near the array from CRUST1.0 (Laske et al., 2013) is also shown
143 in Figure 2 by the dotted lines. The depth of the Moho is at 42 km for the OGS velocity model and
144 also for CRUST1.0 in the region near the array.

145 **Move-out Analysis**

146 Alignment of Moho reflected seismic signals is performed in order to enhance the signal to
147 noise ratio (SNR). Fig. 3 illustrates the move-out corrections performed for the alignment of the
148 Moho-reflected signals.

149 The dashed line in Fig. 3a) is a schematic of Moho reflected arrival-times based on ray tracing
150 for the OGS velocity model (Darold et al., 2015) for a standard focal depth of 5 km. The predicted
151 Moho reflection arrival-times have offsets ranging from 0 to 50 km. The asterisks illustrate the
152 Moho reflection arrival-times for events of different focal depths reported in the OGS earthquake
153 catalog. The offsets are calculated from the latitudes and longitudes of the receivers and OGS
154 located events. To account for event depth variability, each trace is shifted in time by a time
155 difference between the predicted Moho reflection arrival-times ray traced for a 5 km depth source
156 and the OGS reported event depths. Each trace is then move-out corrected by the time between the
157 dashed line and the flat line. In this way, the delay times resulting from offset are compensated
158 for. The total time shift for each trace is denoted by the arrows in Fig. 3a), integrating the time
159 shifts for the variability in both event depth and offset. The Moho reflection arrival-times are then
160 approximately flattened for stacking along the receiver array for a given event.

161 Fig. 3b) illustrates the ray tracing for the Moho reflections. The asterisks and triangles
162 represent seismic events and receiver array, respectively. The schematic ray paths are denoted by
163 black lines between seismic events and receiver array. The move-out corrections then flatten the

164 arrival-times to the zero-offset time for a standard 5 km event depth. This then allows for stacking
165 of the arrivals across the array for each event.

166 **Stacking for Moho Reflections**

167 **Single-Event Stacking**

168 We analyzed the later *P*- and *S*-wave arrivals for the receiver gathers from events within 50
169 km of the center of the array. Move-out corrections and receiver stacking were then applied to
170 identify the Moho reflections on the vertical and horizontal transverse components. Corrections
171 for the reported focal depths were applied to a standard depth of 5 km.

172 Fig. 4 shows receiver gathers for two seismic events recorded on the vertical component by
173 the east-west linear array nodal stations. Each trace is low-pass filtered to 2 Hz and gained by a
174 power of t to approximately equalize the amplitude decay with time. The solid and dashed lines
175 are the predicted arrival-times for the *P* and *PmP* phases from ray tracing, after a move-out
176 correction for the *PmP* arrival-time has been applied. The rightmost traces for each single event
177 receiver gather are the move-out corrected stacked traces. The arrows on the right denote the
178 estimated arrival-times of the *P*, *S*, and *PmP* on the stacked trace.

179 Fig. 5 shows receiver gathers for two events recorded on the transverse component. Each
180 trace is low-pass filtered to 1.5 Hz and gained by a power of t to approximately equalize the
181 amplitude decay with time. The solid and dashed lines are the predicted *S* and *SmS* arrivals after a
182 move-out correction for the predicted *SmS* phase. The rightmost traces in each single-event

183 receiver gather is the move-out corrected stacked traces. The arrows on the right denote the
184 estimated arrival-times of the *S* and *SmS* on the stacked trace.

185 The filtering, gaining, move-out corrections, and stacking are used to bring out the Moho
186 reflected signals. The observed Moho reflection signals could arrive earlier or later than the
187 predicted arrival-times from the ray tracing. The deviation between observed and predicted Moho
188 reflected arrival-times could result from variations in Moho depths, location and focal depth
189 variability in the OGS earthquake catalog and velocity variability.

190 **Multiple-Event Stacking**

191 In order to further enhance the Moho reflection signals, 17 seismic events within 50 km of
192 the center of the array were selected based on signal to noise level and event size to perform
193 multiple-event stacks for the P- and S-wave Moho reflections. We also looked for events with
194 offsets from the array where there was no interference between the Moho reflections and other
195 phases. The selected pre-critical seismic events can be found in the supplementary material with
196 distances less than 50 km from the array, and are shown by the dark black dots in Figure 1.

197 Fig. 6 illustrates the stacking of multiple events on the vertical component and the
198 improvement of stacking by incorporating static and polarity corrections. Each trace on the left in
199 Fig. 6a) is a single-event receiver gather stacking result. The rightmost trace is the multiple-event
200 stacked trace. The line on top of each trace is the trace envelope. The Hilbert transform is used to
201 form the analytic signal which is a complex time signal whose real part is the original signal and

202 imaginary part is the Hilbert transform of the original signal (Shin and Hammond, 2008). The
203 magnitude of analytical signal is the instantaneous amplitude, i.e. the envelope of the original
204 signal.

205 After the envelope is calculated, the local maximum of the envelope around the predicted
206 Moho reflection, within ± 1.5 seconds of the predicted arrival-time is determined. The average of
207 the observed Moho reflection arrival-times is calculated, and each trace is shifted to align the peaks
208 of the envelopes. The standard deviation about the average line is .29 s, and could result from
209 lateral variability of the velocities, variations in the Moho depth, and uncertainties in the event
210 locations and depths.

211 Sign corrections of the waveforms were also applied at the peak of the envelopes. Traces with
212 negative amplitudes at the peak of the envelopes are multiplied by a negative one to account for
213 the variability of polarities, resulting from the event focal mechanisms and possible effects from
214 local structure. The corrected receiver stacked traces are then stacked in Fig. 6b). The dashed line
215 is the predicted moveout-corrected arrival-times from the OGS model, and the solid line is the
216 mean of the envelope peaks. The location of the direct *S*-wave is shown by an arrow. After the
217 static and polarity corrections, the stacked trace is shown on the rightmost trace. The estimated
218 *PmP* is shown by the arrow. Also shown by the lower arrow on the stack in Fig. 6b) is the possible
219 location of the surface reflected *sPmP* arrival, although this is less evident on the individual event
220 stacks.

221 Figure 7 shows a similar plot for the multiple-event stacking on the transverse component.
222 The Moho reflection for the *S*-wave can also be enhanced by the multiple-event stacking after
223 similar static corrections and sign corrections for single-event receiver stacks, where the inferred
224 *SmS* is shown by the arrow. The lower arrow in Fig. 7b) is the possible arrival of the surface
225 reflected *sSmS* arrival, however this is less evident on the individual event stacks.

226 The average absolute deviations about the average lines for the *PmP* and *SmS* arrivals are .29
227 s and .40 s, respectively. The average standard errors for the selected events from the OGS catalog
228 are 0.57 km for the horizontal locations and 1.1 km for the depths. For a 25 km offset and 5 km
229 depth earthquake, the largest arrival-time deviations obtained from ray tracing for the errors in
230 horizontal location and depth are 0.18 s for the *PmP* and 0.32 s for the *SmS*. These are comparable
231 with the deviations about the average lines for the *PmP* and *SmS* arrivals, with additional
232 components of the deviations resulting from lateral velocity variations and Moho depth.

233 The multiple-event stacks are used to identify the Moho reflections from the vertical *P*-waves
234 and transverse *S*-waves. The zero-offset results from multiple-event stacks can then be used to
235 estimate the average *P*- and *S*-wave velocity ratio, V_p/V_s , and the corresponding Poisson's ratio
236 for the crust in this area. The normal moveout corrected *P*- and *S*-wave arrival-times from the
237 multiple-event stacks after static and polarity sign corrections are 12.57 s and 22.28 s for *P*- and
238 *S*-waves, respectively. The uncertainties for the stacked zero-offset Moho reflection arrival-times
239 are approximately 0.15 s on the stacked traces. This results in an average crustal V_p/V_s ratio of
240 $1.77 \pm .02$ and a corresponding Poisson's ratio of $0.266 \pm .009$.

241 The OGS velocity model of Darold et al. (2015) used an assumed V_p/V_s ratio of 1.73. The
242 velocity model from CRUST1.0 (Laske et al., 2013) near the array has a variable V_p/V_s ratio with
243 depth, with an average V_p/V_s for the crust of 1.75. The average Poisson's ratio for the continental
244 crust has been estimated as 0.265 from rock sample measurements (Christensen, 1996). Also an
245 early study by Zandt and Ammon (1995) estimated a Poisson's ratio of 0.27 for platform areas of
246 the continental crust.

247 Receiver functions can be used to estimate the crustal V_p/V_s using the H- κ method (Zhu and
248 Kanamori, 2000). From the EarthScope Automated Receiver Survey (EARS) (Crotwell and
249 Owens, 2005; IRIS, 2010), the V_p/V_s and Poisson's ratio are quite variable in the study area.
250 Individual station values and a map of V_p/V_s values across the U.S. are given by IRIS (2010).
251 Using the broadband stations from the IRIS Community Wavefield Experiment in Oklahoma, the
252 V_p/V_s values range from 1.73 to 2.10 and Poisson's ratios range from 0.25 to 0.35. The V_p/V_s
253 values from receiver functions, however, can have significant variability resulting from difficulties
254 in the measurements of later arrivals of the receiver functions at specific stations. Based on results
255 from well-log information, Schoenball and Ellsworth (2017) used a V_p/V_s of 1.78 to revise the
256 OGS velocity model for their study. This is similar to the average crustal V_p/V_s of 1.77 found in
257 this study from the PmP and SmS arrivals. The modified V_s velocities assuming a V_p/V_s of 1.77
258 is shown by the dashed line in Figure 2.

259 **Time-to-depth conversion**

260 The multiple-event stacking results after corrections are used to perform the time-to-depth
261 conversions. The Moho depth is shown for both *PmP* and *SmS* after time to depth conversions in
262 Figure 8. We use the OGS velocity model as a starting model and adjust the V_p/V_s ratio in order
263 to make Moho depth from the *PmP* and *SmS* arrivals consistent. Deconvolutions are also
264 performed on the multiple-event stacks in order to mitigate the effects of the later arrivals on the
265 *PmP* and *SmS* traces.

266 Figure 8 shows the Moho reflection traces and their deconvolutions with both time and depth.
267 Fig. 8a) shows the *PmP* and decon-*PmP* traces with time. The left trace is the multiple-event stack
268 of the vertical component after static and polarity corrections. A tapering is applied between 9 to
269 11 seconds to mitigate the effect of direct *S* arrivals. Slight filtering is also applied to make the
270 frequency content on the vertical component comparable to that of the transverse component. The
271 right trace in 8a) is the deconvolution to remove the second pulse between 15 to 16 seconds.
272 Assuming that the stacked trace $y(t)$ is comprised of the Moho reflection pulse $r(t)$ and a
273 delayed pulse $a \cdot r(t - \tau)$, where a is the amplitude of the second pulse and τ is the time delay
274 of the second pulse, the stacked trace $y(t)$ can be approximated as

$$275 \quad y(t) = r(t) + a \cdot r(t - \tau) \quad 1.1$$

276 The corresponding Fourier transform can be written as

$$277 \quad Y(\omega) = R(\omega)(1 + ae^{-i\omega\tau}) \quad 1.2$$

278 where ω is the radial frequency. The Fourier transform of $r(t)$, i.e. $R(\omega)$, can then be

279 deconvolved as

$$280 \quad R(\omega) = \frac{(1+ae^{i\omega\tau})Y(\omega)}{(1+ae^{i\omega\tau})(1+ae^{-i\omega\tau})+\varepsilon^2} \quad 1.3$$

281 where ε is a small damping parameter used to stabilize the deconvolution.

282 Fig. 8b) shows the *SmS* and decon-*SmS* traces with time. The left trace is the multiple-event
283 stack of the transverse component after static and polarity corrections. The right trace in 8b) is
284 deconvolution to remove the second pulse between 25 to 26 seconds, in a similar fashion as for
285 the *PmP*.

286 Fig. 8c) shows the *PmP* and decon-*PmP* traces with depth. The OGS P-wave velocity model
287 is used to perform a time-to-depth conversion, where for each point of the time axis, an equivalent
288 depth is found by ray tracing for a source with a 5 km focal depth assuming single scattering from
289 reflectors at depth. The Moho depth calculated from the *P*-wave Moho reflection is $41 \pm .6$ km,
290 where the uncertainty is based on the width of the central pulse of the *PmP* arrival converted to
291 depth. This is slightly shallower than the 42 km Moho depth from the original OGS velocity model.

292 Fig. 8d) shows the *SmS* and decon-*SmS* traces with depth. The Moho depth is converted from
293 time in a similar fashion as for the P-wave traces, and is dependent on the V_s velocity model used.
294 The original OGS velocity model assumed a V_p/V_s ratio of 1.73, but this doesn't result in a
295 consistent Moho depth estimation between the *PmP* and *SmS* traces converted to depth. However,
296 using a V_p/V_s ratio of 1.77 to convert the *SmS* trace to depth results in a consistent Moho depth
297 estimation with the *PmP* trace. Note that converting from time to depth results in a better resolution
298 in depth for the S-wave traces compared to the P-wave traces.

299 There are two possibilities for the second arrivals on the *PmP* and *SmS* traces which arrive
300 later than the Moho reflections, between 9 to 11 seconds on the *PmP* trace in time on the left plot
301 of Fig. 8a) and between 25 to 26 seconds on the *SmS* trace in time on the left plot of Fig. 8b),
302 respectively. The first possibility is that these are primary reflections from a deeper interface. As
303 shown in the OGS velocity model in Figure 2, there could be a potential deeper interface at around
304 50 km in this model.

305 The left traces in Figs. 8c) and 8d) are the time-to-depth conversion of the multiple-event
306 stacks on the vertical and transverse components. The depth range on these plots is shown from
307 35 to 50 km. If the later second pulses are primary reflections from a deeper interface, this interface
308 will be deeper than 50 km shown on Fig. 8c) for the *P*-wave converted to depth and at 48 km on
309 Figure 8d) for the *S*-wave converted to depth. The depth of a possible deeper interface for these
310 later phases is thus inconsistent between the *P*-wave and *S*-wave traces converted to depth. We
311 therefore exclude the possibility that these later arrivals result from a deeper interface.

312 The second possibility is that the later phases are surface reflected phases. However, to be
313 consistent between the *PmP* and *SmS* traces, the later pulse on the *PmP* trace would need to be an
314 *sPmP* arrival and the later phase on the *SmS* trace an *sSmS* arrival. For zero-offset propagation,
315 the amplitude for the *S*-to-*P* conversion at the free surface would be zero. However, the stacked
316 *P*-wave trace is derived from the stacking of traces with non-zero offsets, and this would allow for
317 a non-zero amplitude on the stacked equivalent zero-offset *P*-wave trace. Also, for earthquake
318 sources the *S*-wave amplitudes would be approximately $(V_p/V_s)^3$, or 5.5 times larger in

319 amplitude then the *P*-waves from the source, assuming a $V_p/V_s = 1.77$ (Aki and Richards, 2002).
320 The later arrival on the *P*-wave trace is however still about .2 s later than would be fully consistent
321 with an *sSmS* on the *S*-wave trace. However, this could result from some phase distortion from the
322 processing for the second arrival on the *P*-wave trace. If the later arrivals are surface reflected
323 arrivals, the traces on the right for each of the subplots on Figure 8 would show the results for just
324 the primary reflection arrivals, with the later arrivals removed by deconvolution.

325 Further sources of errors in the results would be from the assumed velocity model. For the
326 analysis performed here, the velocity model in the vicinity of the array is assumed to be laterally
327 homogeneous, and static corrections are implemented to account for small lateral inhomogeneities.
328 For a variation of the velocity model in depth, this would affect the *P*-wave and *S*-wave results in
329 a similar fashion in terms of the inferred average crustal V_p/V_s ratio. However, a slightly faster
330 lower crust than that of the assumed OGS velocity model, as inferred for example by Ratre and
331 Behm (2019), would make the estimates of Moho depths correspondingly deeper.

332 **Wide-angle Moho Reflections**

333 As an illustration of recording wide-angle reflections from the Moho for a large-N array,
334 several seismic events were selected to form composite record sections. The selection of these
335 seismic events was based on several criteria, including background cultural noise level and the
336 magnitude of seismic events. Selected events for the analysis of wide-angle arrivals, with distances
337 between 90 to 135 km from the center of the array, are listed in the supplementary material.

338 The transverse *S*-wave components from five seismic events recorded on the left north-south
339 linear nodal array stations are plotted on the composite record section in Fig 9a). The events are
340 21, 22, 24, 25 and 26 in the Supplemental material. Each trace is low-pass filtered to 1.5 Hz. Fig
341 9b) shows the annotations of several observed seismic phases. The thick solid line and arrows
342 show the predicted *SmS* arrival, where the arrival-times are ray traced from the modified OGS
343 velocity model and the depths in the OGS seismic catalog. A Moho depth of 40 ± 1 km was inferred
344 for the wide-angle modeling of these events with epicenter-to-station distances of 100-135 km
345 from the array for the *S* phases. However due to the depth variability in the catalog, the predicted
346 arrival-times may deviate from the observed arrival-times. The thin solid line and arrows show the
347 direct *S* arrival, which is the first strong seismic phase on the transverse component. The light gray
348 dashed line and arrows show the location of an arrival after the direct *S* but followed by the *SmS*
349 arrival from the Moho at this distance range, which could be a surface reflected direct arrival *sS*,
350 or a surface wave with an apparent speed of 3.45 km/s in a narrow band frequency 0-1.5 Hz (Zhan
351 et al., 2010). The surface reflected Moho reflection phase *sSmS* is also denoted by the solid dashed
352 line and arrows in Fig 9b). The amplitude of this phase varies between events, partly due to the
353 shallow subsurface structure on the source side.

The vertical *P*-wave components from six selected seismic events recorded on the left north-south linear nodal array stations are plotted on the composite record section in Fig 10a). The events are 18, 19, 20, 23, 25 and 26 in the Supplemental material. Each trace is low-pass filtered to 2 Hz. Fig 10b) shows the annotations of several observed seismic phases. The thick solid line and arrows

show the predicted *PmP* arrival, where the arrival-times are ray traced from the modified OGS velocity model and the depth in the OGS seismic catalog. Again, a Moho depth of 40 ± 1 km was inferred for the wide-angle modeling of these events with epicenter-to-station distances of 90 to 135 km from the array for the P phases. The thin solid line and arrows show the direct *P* arrivals. The slight gray dashed line and arrows show the location of an arrival after the direct *P* but followed by the *PmP* arrival from the Moho, which could be the surface reflected directed arrival *pP*. The surface reflected Moho reflection phase *pPmP* is also denoted by the dotted line and arrows in Fig 10b). Due to the smaller energy of *P* wave from earthquakes and the affects from *SV* waves on the vertical component, the *PmP* Moho reflections are less evident than the *SmS* Moho reflections. The difference between the pre-critical and wide-angle Moho depth estimates could result from some lateral variability between the seismic array and the more distant wide-angle events. However, both estimates are shallower than the original OGS model, and this could also result from a somewhat faster lower crust.

354 **Conclusions**

355 The deployments of large-N seismic arrays have become increasingly popular, enabling
356 advances in subsurface imaging. In this study, the *P*- and *S*-wave later arrivals from local seismic
357 events near the large-N IRIS Community Wavefield Experiment in Oklahoma are used to illustrate
358 the analysis of Moho reflections and average crustal thickness and V_p/V_s ratio near the array. The
359 pre-critical *PmP* and *SmS* Moho reflections for events within 50 km of the center of the array were

360 first found on single-event stacks by applying normal moveout corrections, low pass filtering and
361 gaining methods. Multiple-event stacks were then applied to further enhance the Moho reflection
362 signals from the stacking of the single-event receiver gathers. Static corrections and polarity
363 corrections were applied to account for lateral variability of Moho depth and velocity structure,
364 and uncertainties in the event locations and focal depths. The arrival-times of the *PmP* and *SmS*
365 on multiple-event stacked traces after NMO, static, and polarity corrections were used to estimate
366 an average crustal V_p/V_s ratio of $1.77 \pm .02$, with a Poisson's ratio of $0.266 \pm .009$ near the array.
367 The inferred crustal V_p/V_s and Poisson's ratio are in good agreement with the previous studies for
368 the average continental crust, although the results in the study area from receiver functions are
369 more variable. Using a modified Oklahoma Geological Survey (OGS) velocity model with this
370 Poisson's ratio, the time-to-depth converted *PmP* and *SmS* arrivals resulted in a Moho depth of 41
371 $\pm .6$ km, which is slightly shallower than the 42 km for the original OGS model.

372 For selected events at epicenter-to-station distances of 90 to 135 km, the modeling of wide-
373 angle arrivals provided additional constraints, and a Moho depth of 40 ± 1 km was inferred. The
374 difference between the pre-critical and wide-angle Moho depth estimates could result from some
375 lateral variability between the seismic array and the more distant wide-angle events, as well as
376 event depth uncertainties. However, both estimates are slightly shallower than the original OGS
377 model, and this could also result from a somewhat faster lower crust.

378 This study shows that local seismic events, including induced events in areas with less natural
379 background seismicity, can be used estimate properties and structure of the crust, which can then

380 be used to better understand the tectonics of a given region. The recording of local seismicity on
381 large-N arrays provides increased lateral phase coherence and this allows for better identification
382 of both pre-critical and wide-angle reflected arrivals.

383 **Data and Resources**

384 The seismic waveform data used in this study were collected as part of the IRIS Community
385 Wavefield Experiment in Oklahoma. Data can be obtained from the IRIS Data Management Center
386 at www.iris.edu (last accessed February 2020). Supplemental Material for this article includes a
387 list of the seismic events used for this study. The hypocenter data for the events are from the
388 Oklahoma Geological Survey at <http://wichita.ogs.ou.edu/eq/catalog/2016/2016.csv> (last accessed
389 February 2020).

390 MATLAB software was used for the visualization, and several codes were modified from the
391 CREWES MATLAB toolbox of the Consortium for Research in Elastic Wave Exploration
392 Seismology, University of Calgary, Calgary, Alberta, CANADA.

393

394 **Acknowledgments**

395 The authors thank the two anonymous Reviewers, The Associate Editor, Dan McNamara, and the
396 Editor for their constructive reviews, which substantially improved the manuscript. The study was

397 partially supported by US National Science Foundation Grant EAR-1839322, and a Purdue EAPS
398 travel grant for the first author.

399 **References**

- 400 Aki, K. and P.G. Richards (2002). *Quantitative Seismology*, University Science Books.
- 401 Anderson, K., J. Sweet, and B. Woodward (2016). IRIS community wavefield experiment in
402 Oklahoma, *Inc. Res. Institutions Seismol. Other/Seismic Netw.*, doi: 10.7914/SN/YW_2016.
- 403 Brenguier, F. et al. (2016). Toward 4D Noise-Based Seismic Probing of Volcanoes: Perspectives
404 from a Large- N Experiment on Piton de la Fournaise Volcano, *Seismol. Res. Lett.* **87**, no. 1,
405 15–25, doi: 10.1785/0220150173.
- 406 Carbonell, R., A. Levander, and R. Kind (2013). The Mohorovičić discontinuity beneath the
407 continental crust: An overview of seismic constraints, *Tectonophysics* **609**, 353–376, doi:
408 10.1016/j.tecto.2013.08.037.
- 409 Christensen, N. I. (1996). Poisson’s ratio and crustal seismology, *J. Geophys. Res. Solid Earth* **101**,
410 no. B2, 3139–3156, doi: 10.1029/95JB03446.
- 411 Cook, F. A., D. J. White, A. G. Jones, D. W. S. Eaton, J. Hall, and R. M. Clowes (2010). How the
412 crust meets the mantle: Lithoprobe perspectives on the Mohorovičić discontinuity and crust–
413 mantle transition, in special issue on the theme Lithoprobe - parameters, processes, and the
414 evolution, *Can. J. Earth Sci.* **47**, no. 4, 315–351, doi: 10.1139/E09-076.
- 415 Crotwell, H. P., and T. J. Owens (2005). Automated Receiver Function Processing, *Seismol. Res.*
416 *Lett.* **76**, no. 6, 702–709, doi: 10.1785/gssrl.76.6.702.
- 417 Darold, A. P., A. A. Holland, J. K. Morris, and A. R. Gibson (2015). Oklahoma earthquake
418 summary report 2014, *Okla. Geol. Surv. Open-File Rept. OF1-2015*, 1–46.
- 419 Eddy, A.C. and S.H. Harder, (2018). Correlation of local earthquakes to form a reflection image
420 beneath the IRIS Community Wavefield Experiment, Grant County, Oklahoma, *Trans. Am.*
421 *Geophys. Union*, AGU Fall Annual Meeting, Dec. 10-14, 2018, Washington DC.
- 422 Ellsworth, W. L. (2013). Injection-Induced Earthquakes, *Science* **341**, no. 6142, 1225942–1225942,
423 doi: 10.1126/science.1225942.
- 424 Evamzia, D., J. Pulliam, R. Ainsworth, H. Gurrola, and K. Pratt (2014). Seismic Vp & Vs
425 tomography of Texas & Oklahoma with a focus on the Gulf Coast margin, *Earth and*
426 *Planetary Sci. Lett.* **402**, 148-156, doi: 10.1016/j.epsl.2013.12.027.
- 427 Fan, W., and J. J. McGuire (2018). Investigating microearthquake finite source attributes with IRIS

- 428 Community Wavefield Demonstration Experiment in Oklahoma, *Geophys. J. Int.* **214**, no. 2,
429 1072–1087, doi: 10.1093/gji/ggy203.
- 430 Freed, D. (2008). Cable-free nodes: The next generation land seismic system, *Lead. Edge* **27**, no.
431 7, 878–881, doi: 10.1190/1.2954027.
- 432 Glasgow, M. E., B. Schmandt, and S. M. Hansen (2018). Upper crustal low-frequency seismicity
433 at Mount St. Helens detected with a dense geophone array, *J. Volcanol. Geotherm. Res.* **358**,
434 329–341, doi: 10.1016/j.jvolgeores.2018.06.006.
- 435 Griffin, J.D., R.L. Nowack, W.P. Chen and T.L. Tseng (2011). Velocity structure of the Tibetan
436 lithosphere: Constraints from P-wave travel-times of regional earthquakes, *Bull. Seism. Soc.*
437 *Am.* **101**, no. 4, 1938-1947, doi: 10.1785/0120100229.
- 438 Hansen, S. M., and B. Schmandt (2015). Automated detection and location of microseismicity at
439 Mount St. Helens with a large-N geophone array, *Geophys. Res. Lett.* **42**, no. 18, 7390–7397,
440 doi: 10.1002/2015GL064848.
- 441 Hansen, S. M., B. Schmandt, A. Levander, E. Kiser, J. E. Vidale, G. A. Abers, and K. C. Creager
442 (2016). Seismic evidence for a cold serpentinized mantle wedge beneath Mount St Helens,
443 *Nat. Commun.* **7**, no. 1, 13242, doi: 10.1038/ncomms13242.
- 444 Harder, S.H. and A.C. Eddy (2017). Migrating local earthquake interferometric data from the IRIS
445 Community Wavefield Experiment, Oklahoma, *Trans. Am. Geophys. Union*, AGU Fall
446 Annual Meeting, New Orleans, LA.
- 447 Hillers, G., P. Roux, M. Campillo, and Y. Ben-Zion (2016). Focal spot imaging based on zero lag
448 cross-correlation amplitude fields: Application to dense array data at the San Jacinto fault
449 zone, *J. Geophys. Res. Solid Earth* **121**, no. 11, 8048–8067, doi: 10.1002/2016JB013014.
- 450 Hincks, T., W. Aspinall, R. Cooke, and T. Gernon (2018). Oklahoma’s induced seismicity strongly
451 linked to wastewater injection depth, *Science* **359**, no. 6381, 1251–1255, doi:
452 10.1126/science.aap7911.
- 453 Inamomri, T., S. Horiuchi, and A. Hasegawa (1992). Location of mid-crustal reflectors, by a
454 reflection method using aftershock waveform data in the focal area of the 1984 Western
455 Nagano Prefecture earthquake, *J. Phys. Earth* **40**, 379-393.
- 456 IRIS, DMC (2010). Data Services Products: EARS EarthScope Automated Receiver Survey, doi:
457 10.17611/DP/EARS.1

- 458 Johnson, K. S. (2008). Geologic history of Oklahoma. Earth sciences and mineral resources of
459 Oklahoma: Oklahoma Geological Survey, Educational Publication, 9, 3-5.
- 460 Karplus, M., and B. Schmandt (2018). Preface to the Focus Section on Geophone Array
461 Seismology, *Seismol. Res. Lett.* **89**, no. 5, 1597–1600, doi: 10.1785/0220180212.
- 462 Keranen, K. M., M. Weingarten, G. A. Abers, B. A. Bekins, and S. Ge (2014). Sharp increase in
463 central Oklahoma seismicity since 2008 induced by massive wastewater injection, *Science*
464 **345**, no. 6195, 448–451, doi: 10.1126/science.1255802.
- 465 Kiser, E., A. Levander, C. Zelt, B. Schmandt, and S. Hansen (2019). Upper Crustal Structure and
466 Magmatism in Southwest Washington: V_p , V_s , and V_p / V_s Results From the iMUSH
467 Active-Source Seismic Experiment, *J. Geophys. Res. Solid Earth* **124**, no. 7, 7067–7080, doi:
468 10.1029/2018JB016203.
- 469 Kiser, E., I. Palomeras, A. Levander, C. Zelt, S. Harder, B. Schmandt, S. Hansen, K. Creager, and
470 C. Ulberg (2016). Magma reservoirs from the upper crust to the Moho inferred from high-
471 resolution V_p and V_s models beneath Mount St. Helens, Washington State, USA, *Geology*
472 **44**, no. 6, 411–414, doi: 10.1130/G37591.1.
- 473 Langenbruch, C., and M. D. Zoback (2016). How will induced seismicity in Oklahoma respond to
474 decreased saltwater injection rates?, *Sci. Adv.* **2**, no. 11, e1601542, doi:
475 10.1126/sciadv.1601542.
- 476 Laske, G., G. Masters, Z. Ma, and M. Pasyanos (2013). Update on CRUST1.0---A 1-degree global
477 model of Earth's crust, *Geophys. Res. Abstracts*, 15, Abstract EGU2013-2658, 2013.
- 478 Levander, A., and G. Nolet (Eds.) (2005). *Seismic Earth: Array Analysis of Broadband*
479 *Seismograms*, Geophysical Monograph Series, **157**, American Geophysical Union,
480 Washington, DC, 252 pp.
- 481 Li, C., Z. Li, Z. Peng, C. Zhang, N. Nakata, and T. Sickbert (2018). Long-Period Long-Duration
482 Events Detected by the IRIS Community Wavefield Demonstration Experiment in Oklahoma:
483 Tremor or Train Signals?, *Seismol. Res. Lett.* **89**, no. 5, 1652–1659, doi: 10.1785/0220180081.
- 484 Li, Z., Z. Peng, D. Hollis, L. Zhu, and J. McClellan (2018). High-resolution seismic event detection
485 using local similarity for Large-N arrays, *Sci. Rep.* **8**, no. 1, 1646, doi: 10.1038/s41598-018-
486 19728-w.
- 487 Lin, F.-C., D. Li, R. W. Clayton, and D. Hollis (2013). High-resolution 3D shallow crustal structure
488 in Long Beach, California: Application of ambient noise tomography on a dense seismic array,

- 489 *Geophysics* **78**, no. 4, Q45–Q56, doi: 10.1190/geo2012-0453.1.
- 490 Marsh, S. (2018). Development of a state-wide velocity profile in Oklahoma using ambient noise
491 seismic tomography, M.S. Thesis, University of Oklahoma, Norman Ok.
- 492 Mechie, J., W. Zhao, M.S. Karplus, Z. Wu, R. Meissner et al. (2012). Crustal shear (S) velocity
493 and Poisson's ratio structure along the INDEPTH IV profile in northeast Tibet as derived from
494 wide-angle data, *Geophys. J. Int.* **191**, 369–384, doi: 10.1111/j.1365-246X.2012.05616.1.
- 495 Mori, J. and D. Helmberger (1996). Large-amplitude Moho reflections (*SmS*) from Landers
496 aftershocks, Southern California, *Bull. Seism. Soc. Am.* **86**, No. 6, 1845–1852.
- 497 Nakata, N., J. P. Chang, J. F. Lawrence, and P. Boué (2015). Body wave extraction and tomography
498 at Long Beach, California, with ambient-noise interferometry, *J. Geophys. Res. Solid Earth*
499 **120**, no. 2, 1159–1173, doi: 10.1002/2015JB011870.
- 500 Nishitsuji, Y., E. Ruigrok, M. Gomez, K. Wapenaar, and D. Draganov (2016). Reflection imaging
501 of aseismic zones of the Nazca slab by global-phase seismic interferometry, *Interpretation* **4**,
502 no. 3, SJ1–SJ16, doi: 10.1190/INT-2015-0225.1.
- 503 Nowack, R. L., W.-P. Chen, and T.-L. Tseng (2010). Application of Gaussian-Beam Migration to
504 Multiscale Imaging of the Lithosphere beneath the Hi-CLIMB Array in Tibet, *Bull. Seismol.*
505 *Soc. Am.* **100**, no. 4, 1743–1754, doi: 10.1785/0120090207.
- 506 OGS Earthquake Catalog (2016) <http://wichita.ogs.ou.edu/eq/catalog/2016/2016.csv> (last
507 accessed February 2020).
- 508 Pei, S., Z. Peng and X. Chen (2018). Locations of injection-induced earthquakes in Oklahoma
509 controlled by crustal structures, *J. Geophys. Res. Solid Earth* **123**, 2332–2344, do:
510 10.1002/2017JB014983.
- 511 Prodehl, C., and W. D. Mooney (2012). Exploring the Earth's Crust—History and Results of
512 Controlled-Source Seismology, *Geol. Soc. Am. Memoirs* **208**, The Geological Society of
513 America, Boulder, CO, 764 pp.
- 514 Qin, L., Y. Ben-Zion, H. Qiu, P.-E. Share, Z. E. Ross, and F. L. Vernon (2018). Internal structure
515 of the San Jacinto fault zone in the trifurcation area southeast of Anza, California, from data
516 of dense seismic arrays, *Geophys. J. Int.* **213**, no. 1, 98–114, doi: 10.1093/gji/ggx540.
- 517 Quiros, D.A., L.D. Brown, K.K. Davenport, J.A. Hole et al. (2017). Reflection imaging with
518 earthquake sources and dense arrays, *J. Geophys. Res.* **122**, 3076–3098, doi:

- 519 10.1002/2016JB013677.
- 520 Ratre, P. and M. Behm (2019). A comprehensive seismic 3D model of the central Oklahoma crust
521 from local earthquake waveforms: implications for the mid-continent rift (MCR), *Trans.*
522 *Am. Geophys. Union*, AGU Fall Annual Meeting, Dec. 9-13, 2019, San Francisco, CA.
- 523 Riahi, N., and P. Gerstoft (2015). The seismic traffic footprint: Tracking trains, aircraft, and cars
524 seismically, *Geophys. Res. Lett.* **42**, no. 8, 2674–2681, doi: 10.1002/2015GL063558.
- 525 Ringler, A. T., R. E. Anthony, M. S. Karplus, A. A. Holland, and D. C. Wilson (2018). Laboratory
526 Tests of Three Z-Land Fairfield Nodal 5-Hz, Three-Component Sensors, *Seismol. Res. Lett.*
527 **89**, no. 5, 1601–1608, doi: 10.1785/0220170236.
- 528 Rondenay, S. (2009). Upper Mantle Imaging with Array Recordings of Converted and Scattered
529 Teleseismic Waves, *Surv. Geophys.* **30**, nos. 4–5, 377–405, doi: 10.1007/s10712-009-9071-5.
- 530 Roux, P., L. Moreau, A. Lecointre, G. Hillers, M. Campillo, Y. Ben-Zion, D. Zigone, and F. Vernon
531 (2016). A methodological approach towards high-resolution surface wave imaging of the San
532 Jacinto Fault Zone using ambient-noise recordings at a spatially dense array, *Geophys. J. Int.*
533 **206**, no. 2, 980–992, doi: 10.1093/gji/ggw193.
- 534 Ruigrok, E., and K. Wapenaar (2012). Global-phase seismic interferometry unveils P-wave
535 reflectivity below the Himalayas and Tibet, *Geophys. Res. Lett.* **39**, no. 11, n/a-n/a, doi:
536 10.1029/2012GL051672.
- 537 Schmandt, B., and R. W. Clayton (2013). Analysis of teleseismic P waves with a 5200-station array
538 in Long Beach, California: Evidence for an abrupt boundary to Inner Borderland rifting, *J.*
539 *Geophys. Res. Solid Earth* **118**, no. 10, 5320–5338, doi: 10.1002/jgrb.50370.
- 540 Schoenball, J. and W.L. Ellsworth (2017). Waveform-relocated earthquake catalog for Oklahoma
541 and Southern Kansas illuminate the regional fault network, *Seism. Res. Lett.* **88**, 1252-11258,
542 doi: 10.1785/0220170083.
- 543 Shen, W. and M.H. Ritzwoller (2016). Crustal and uppermost mantle structure beneath the United
544 States, *J. Geophys. Res. Solid Earth* **121**, 4306-4342, doi: 10.1002/2016JB012887.
- 545 Shin, K., and J. Hammond (2008). *Fundamentals of signal processing for sound and vibration*
546 *engineers*, John Wiley & Sons, New Jersey, 90-93.
- 547 Skoumal, R.J., J.O. Kaven and J.I. Walter (2019). Characterizing seismogenic fault structures in
548 Oklahoma using a relocated template-matching catalog, *Seism. Res. Lett.* **90**, 1535-1540, doi:

- 549 10.1785/0220190045.
- 550 Sweet, J. R. et al. (2018). A Community Experiment to Record the Full Seismic Wavefield in
551 Oklahoma, *Seismol. Res. Lett.* **89**, no. 5, 1923–1930, doi: 10.1785/0220180079.
- 552 Thompson, D. A., N. Rawlinson, and H. Tkalčić (2019). Testing the limits of virtual deep seismic
553 sounding via new crustal thickness estimates of the Australian continent, *Geophys. J. Int.* **218**,
554 no. 2, 787–800, doi: 10.1093/gji/ggz191.
- 555 Tseng, T.-L., W.-P. Chen, and R. L. Nowack (2009). Northward thinning of Tibetan crust revealed
556 by virtual seismic profiles, *Geophys. Res. Lett.* **36**, no. 24, L24304, doi:
557 10.1029/2009GL040457.
- 558 Walsh, F. R., and M. D. Zoback (2015). Oklahoma’s recent earthquakes and saltwater disposal, *Sci.*
559 *Adv.* **1**, no. 5, e1500195, doi: 10.1126/sciadv.1500195.
- 560 Walter, J.I., P. Ogwari, A. Thiel , F. Ferrer, et al., (2020). The Oklahoma Geological Survey
561 Statewide Seismic Network, *Seismol. Res. Lett.* **91**, no. 2A, 611-621, doi:
562 10.1785/0220190211.
- 563 Wang, Z., P. Persaud and M. Behm (2019). Investigation of the crust in Oklahoma from broadband
564 teleseismic receiver function, *Trans. Am. Geophysical Union*, AGU Fall Annual Meeting, Dec.
565 9-13, 2019, San Francisco CA.
- 566 Wang, Y., A. Allam, and F. Lin (2019). Imaging the Fault Damage Zone of the San Jacinto Fault
567 Near Anza With Ambient Noise Tomography Using a Dense Nodal Array, *Geophys. Res. Lett.*
568 **46**, no. 22, 12938–12948, doi: 10.1029/2019GL084835.
- 569 Wang, Y., F.-C. Lin, B. Schmandt, and J. Farrell (2017). Ambient noise tomography across Mount
570 St. Helens using a dense seismic array, *J. Geophys. Res. Solid Earth* **122**, no. 6, 4492–4508,
571 doi: 10.1002/2016JB013769.
- 572 Ward, K. M., and F. Lin (2017). On the Viability of Using Autonomous Three-Component Nodal
573 Geophones to Calculate Teleseismic Ps Receiver Functions with an Application to Old
574 Faithful, Yellowstone, *Seismol. Res. Lett.* **88**, no. 5, 1268–1278, doi: 10.1785/0220170051.
- 575 Weingarten, M., S. Ge, J. W. Godt, B. A. Bekins, and J. L. Rubinstein (2015). High-rate injection
576 is associated with the increase in U.S. mid-continent seismicity, *Science* **348**, no. 6241, 1336–
577 1340, doi: 10.1126/science.aab1345.
- 578 Wu, S.-M., K. M. Ward, J. Farrell, F.-C. Lin, M. Karplus, and R. B. Smith (2017). Anatomy of Old

- 579 Faithful From Subsurface Seismic Imaging of the Yellowstone Upper Geyser Basin, *Geophys.*
580 *Res. Lett.* **44**, no. 20, 10,240-10,247, doi: 10.1002/2017GL075255.
- 581 Yu, C.-Q., W.-P. Chen, and R. D. van der Hilst (2013). Removing source-side scattering for virtual
582 deep seismic sounding (VDSS), *Geophys. J. Int.* **195**, no. 3, 1932–1941, doi:
583 10.1093/gji/ggt359.
- 584 Zandt, G., and C. J. Ammon (1995). Continental crust composition constrained by measurements
585 of crustal Poisson’s ratio, *Nature* **374**, no. 6518, 152–154, doi: 10.1038/374152a0.
- 586 Zhu, H. (2018). Crustal wave speed structure of North Texas and Oklahoma based on ambient
587 noise cross-correlation functions and adjoint tomography, *Geophys. J. Int.* **214**, 716-730,
588 doi:10.1093/gji/ggy169.
- 589 Zhu, L., and H. Kanamori (2000). Moho depth variation in southern California from teleseismic
590 receiver functions, *J. Geophys. Res. Solid Earth* **105**, no. B2, 2969–2980, doi:
591 10.1029/1999JB900322.

592 Qicheng Zeng¹
593 Robert L. Nowack¹
594 Department of Earth, Atmospheric, and Planetary Sciences
595 550 Stadium Mall Dr.
596 Purdue University
597 West Lafayette IN 47907 USA
598 qczeng95@gmail.com
599 nowack@purdue.edu

600 **List of Figure Captions**

601 **Figure 1.** a) Map of near offset seismic events from the OGS catalog over a period from June 24
602 to July 20, 2016. The events are denoted by dots, and the dark black dots were selected for the
603 analysis. The dashed circles have radii of 10 km, 30 km and 50 km from a central station of the
604 array of the IRIS Community Wavefield Experiment. The right inset map shows the geometry of
605 the receivers in the array. The triangles are the north-south and east-west linear nodal array stations,
606 the small square denoted stations from the nodal gradiometer array, and the squares are the
607 broadband stations (Sweet et al., 2018). b) shows the major geologic structures in Oklahoma
608 (adapted from Johnson 2008). The triangle in central north Oklahoma denotes the location of the
609 array. The dashed circles around the triangle have radii of 10 km, 30 km and 50 km from a central
610 station of the array.

611 **Figure 2.** Reference velocity models of the study area. The velocity model from the Oklahoma
612 Geological Survey (Darold et al., 2015) is denoted by solid lines, with S wave velocity on the left
613 and P wave velocity on the right. The OGS velocity model assume a constant 1.73 V_p/V_s ratio.
614 Using a V_p/V_s of 1.77 instead, we derive a new shear wave velocity model, denoted the dashed
615 line. The velocity model from CRUST1.0 (Laske et al., 2013) is shown by the dotted lines for
616 comparison.

617 **Figure 3.** a) Move-out corrections for the Moho reflections. The dashed line is the predicted Moho
618 reflected arrival-times for a reference 5 km depth source, from the OGS velocity model (Darold et
619 al., 2015). b) shows a schematic diagram of the Moho reflected rays. The asterisks represent

620 seismic events with different offsets and focal depths from the receiver array depicted by triangles.

621 Move-out corrections are performed for each seismic event and receiver pair. The move-out time

622 shifts flatten the Moho reflected arrivals and also correct for the event depths to a standard depth.

623 **Figure 4.** a) A single-event receiver gather of the vertical components recorded by the east-west

624 linear array nodal stations for event 5 in the supplementary material. Each trace is low-pass filtered

625 to 2 Hz and gained by a power of t to approximately equalize the amplitude decay with time. The

626 solid and dashed lines are the predicted arrival times for the P and PmP from ray tracing after a

627 move-out correction for the PmP arrival. The rightmost trace is the event stack. The arrows on the

628 right denotes the observed arrival-times of the P , S , and PmP on the stacked trace. b) is a similar

629 plot for event 9.

630 **Figure 5.** a) A single-event receiver gather of the transverse component recorded by east-west

631 linear array stations for event 4 in the supplementary material. Each trace is low-pass filtered to

632 1.5 Hz and gained by a power of t to approximately equalize the amplitudes in time. The solid and

633 dashed lines are the predicted S and SmS arrivals after a move-out correction for the SmS arrival-

634 time. The rightmost trace in each single-event receiver gather is the stack. b) is a similar plot for

635 event 8.

636 **Figure 6.** a) shows the multiple-event stacking of the vertical component stacks. Each trace on the

637 left is a single-event receiver stack result. The rightmost trace is the multiple-event stacked trace.

638 For each trace the envelope is also shown. The dashed line is the predicted time of the normal

639 moveout corrected predicted PmP arrivals for the OGS model. The direct S is also shown for one

640 event. b) shows the multiple-event stack of the vertical component after static and polarity
641 corrections. The dashed line is the predicted moveout corrected time of the PmP from the OGS
642 model. The solid line is the average of the envelope peaks denoting the predicted Moho reflection
643 time. The direct S wave is shown by arrows in both a) and b). Static corrections and polarity
644 corrections are applied to the individual traces prior to stacking, with the stack shown on the right.
645 The inferred PmP arrival is shown by an arrow. The lower arrow on the stack could be the location
646 of the surface reflected $sPmP$ arrival.

647 **Figure 7.** a) shows the multiple-event stacking of the transverse component stacks. Each trace on
648 the left is a single-event receiver stack result. The dashed line is the predicted time for the moveout
649 corrected SmS from the OGS model. The rightmost trace is the multiple-event stacked trace. b)
650 shows the multiple-event stack of the transverse component after static and polarity corrections.
651 The dashed line is the predicted time for the moveout corrected SmS from the OGS model. The
652 solid line is the average of the envelope peaks denoting the inferred Moho reflection time. Static
653 corrections and polarity corrections are applied to the individual traces prior to stacking, with the
654 stack shown on the right. The inferred SmS arrival is shown by an arrow. The lower arrow on the
655 stack could be the location of the surface reflected $sSmS$ arrival.

656 **Figure 8.** a) shows the PmP and decon- PmP traces with time. The left trace is the multiple event
657 stack of the vertical component after static and polarity corrections. A tapering is applied between
658 9 to 11 seconds to mitigate the effect of direct S arrivals. Slight filtering is also applied to make
659 the frequency content on the vertical component comparable to that of the transverse component.

660 The right trace is the deconvolution of the left trace to remove the later pulse between 15 to 16
661 seconds. b) shows the *SmS* and decon-*SmS* traces with time. The left trace is the multiple-event
662 stack of the transverse component after static and polarity corrections. The right trace is the
663 deconvolution of the left trace to remove the later pulse between 25 to 26 seconds. c) shows the
664 *PmP* and decon-*PmP* traces with depth. The OGS *P* wave velocity model is used to perform the
665 time to depth conversion. The Moho depth obtained for the *P*-wave Moho reflection is at 41 km.
666 d) shows the *SmS* and decon-*SmS* traces with depth. The S-wave velocity calculated from OGS *P*
667 wave velocity using a 1.77 V_p/V_s ratio is used to perform the time to depth conversion. The Moho
668 depth obtained from the S-wave Moho reflection is also at 41 km consistent with the estimate from
669 the *PmP* traces with depth.

670 **Figure 9.** a) Composite record section of the wide-angle *SmS* Moho reflections on the transverse
671 component, recorded on the left north-south linear nodal array stations. Each trace is low-pass
672 filtered to 1.5 Hz. The inset map shows the location of earthquakes, denoted by gray dots. The
673 black dots are selected for the plot. b) shows the composite record section with identified phase
674 shown. The thick solid line and arrows show the predicted *SmS* arrival. The arrival-times are ray
675 traced from the modified OGS model and the depths in the OGS seismic catalog. The thin solid
676 line and arrows show the direct *S* arrival. The surface reflected Moho reflection phase *sSmS* is also
677 denoted by the dotted line and arrows. The light gray dashed line and arrow show either a surface
678 reflected direct wave *sS* or a surface wave with a 3.45 km/s apparent velocity in a narrow frequency
679 band.

680 **Figure 10.** a) Composite record section of the wide-angle PmP Moho reflections on the vertical
681 component, recorded on the left north-south linear nodal array stations. Each trace is low-pass
682 filtered to 2 Hz. The inset map shows the location of earthquakes, denoted by gray dots. The black
683 dots are selected for the analysis. b) shows the composite record section with identified phase
684 shown. The thick solid line and arrows show the predicted PmP arrival. The arrival-times are ray
685 traced from the modified OGS velocity model and the depth in the OGS seismic catalog. The thin
686 solid line and arrows show the direct P arrival. The surface reflected Moho reflection phase $pPmP$
687 is also denoted by the dotted line and arrows. The light gray dashed line and arrows show a possible
688 surface reflected direct wave pP .

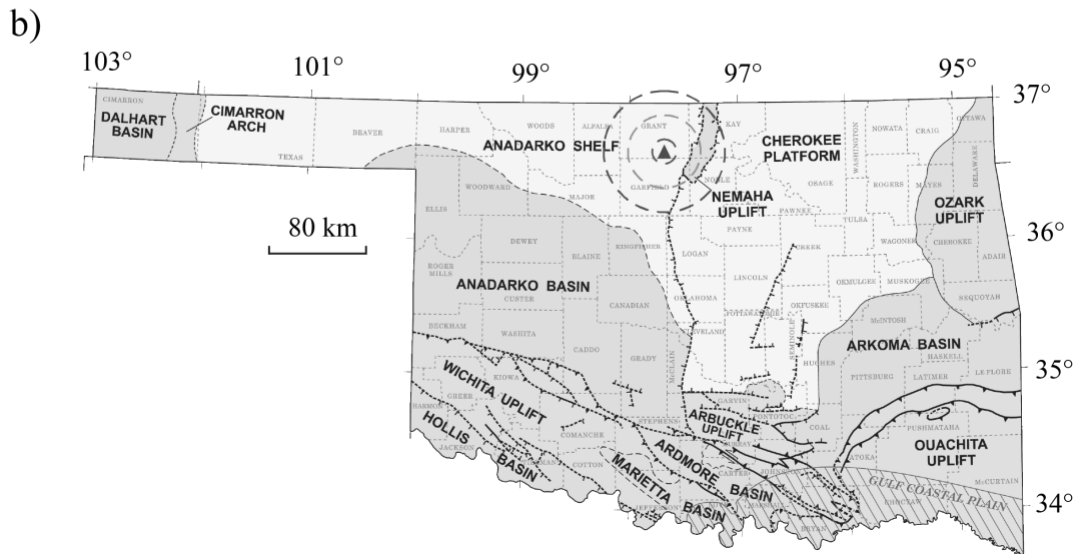
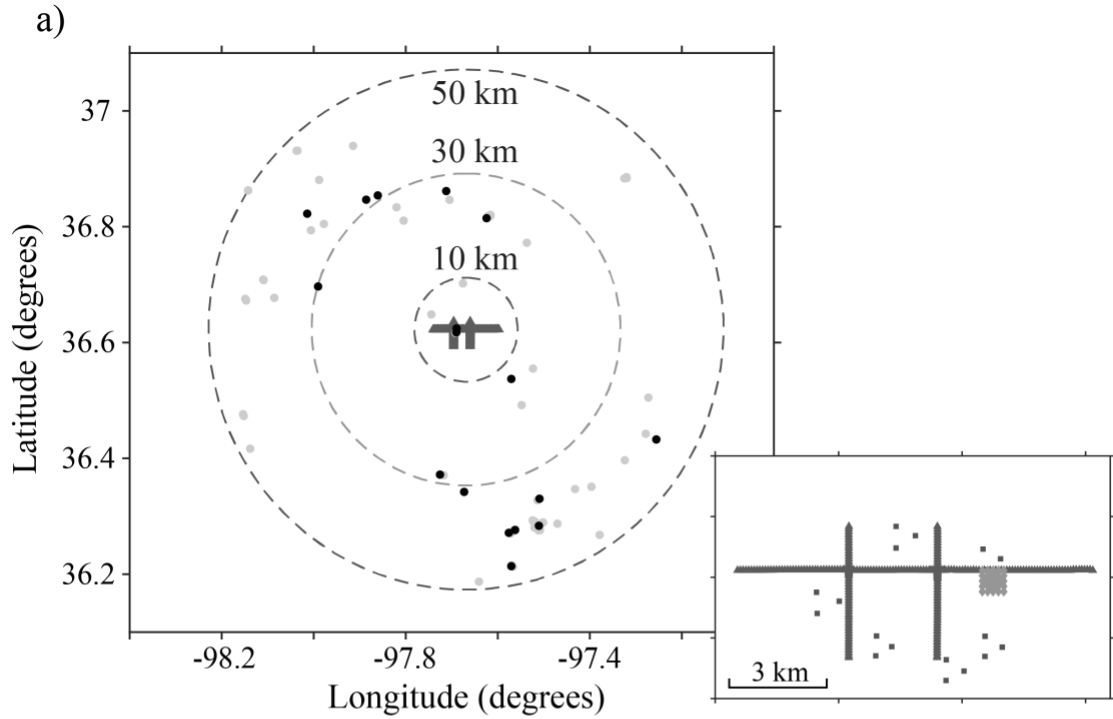


Figure 1. a) Map of near offset seismic events from the OGS catalog over a period from June 24 to July 20, 2016. The events are denoted by dots, and the dark black dots were selected for the analysis. The dashed circles have radii of 10 km, 30 km and 50 km from a central station of the array of the IRIS Community Wavefield Experiment. The right inset map shows the geometry of the receivers in the array. The triangles are the north-south and east-west linear nodal array stations,

the small square denoted stations from the nodal gradiometer array, and the squares are the broadband stations (Sweet et al., 2018). b) shows the major geologic structures in Oklahoma (adapted from Johnson 2008). The triangle in central north Oklahoma denotes the location of the array. The dashed circles around the triangle have radii of 10 km, 30 km and 50 km from a central station of the array.

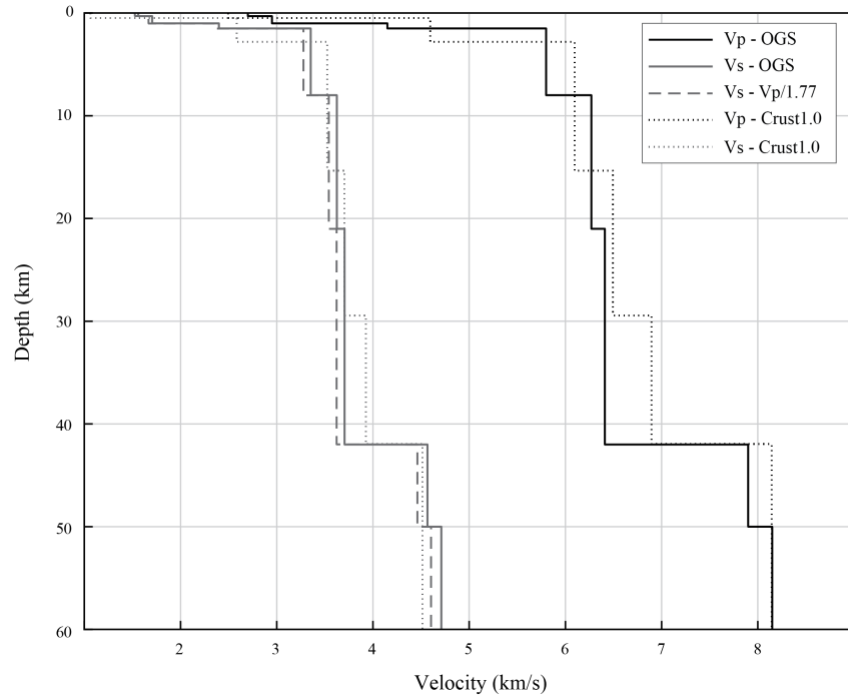


Figure 2. Reference velocity models of the study area. The velocity model from the Oklahoma Geological Survey (Darold et al., 2015) is denoted by solid lines, with S wave velocity on the left and P wave velocity on the right. The OGS velocity model assume a constant 1.73 V_p/V_s ratio. Using a V_p/V_s of 1.77 instead, we derive a new shear wave velocity model, denoted the dashed line. The velocity model from CRUST1.0 (Laske et al., 2013) is shown by the dotted lines for comparison.

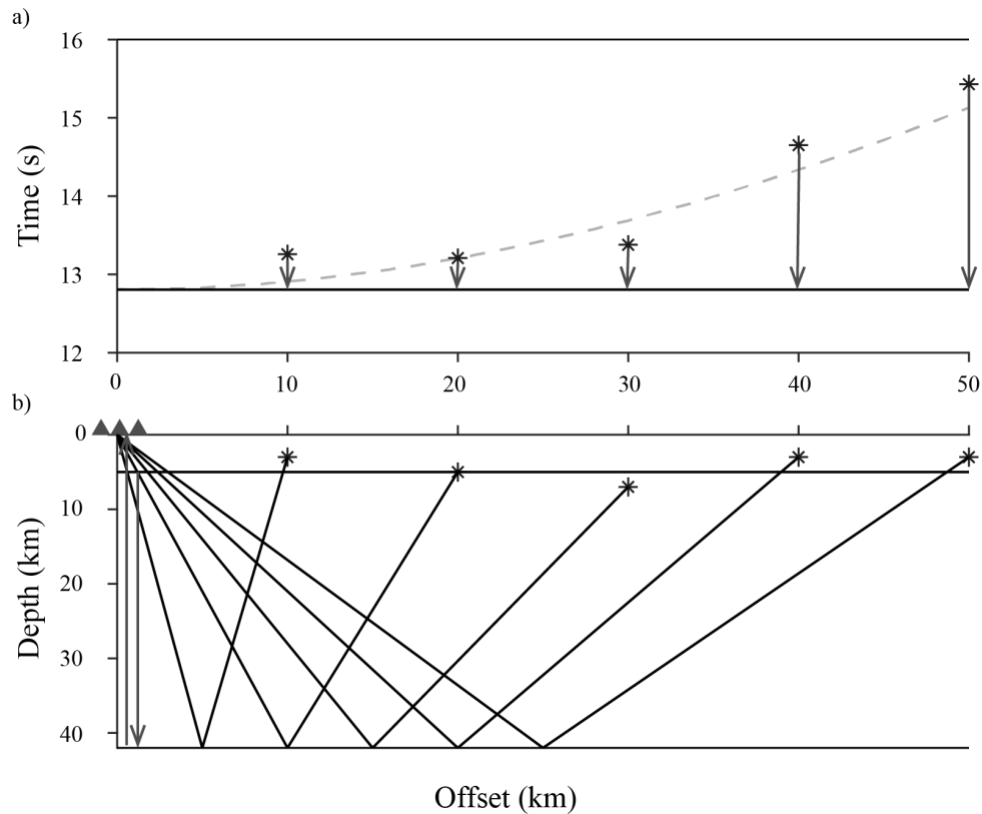


Figure 3. a) Move-out corrections for the Moho reflections. The dashed line is the predicted Moho reflected arrival-times for a reference 5 km depth source, from the OGS velocity model (Darold et al., 2015). b) shows a schematic diagram of the Moho reflected rays. The asterisks represent seismic events with different offsets and focal depths from the receiver array depicted by triangles. Move-out corrections are performed for each seismic event and receiver pair. The move-out time shifts flatten the Moho reflected arrivals and also correct for the event depths to a standard depth.

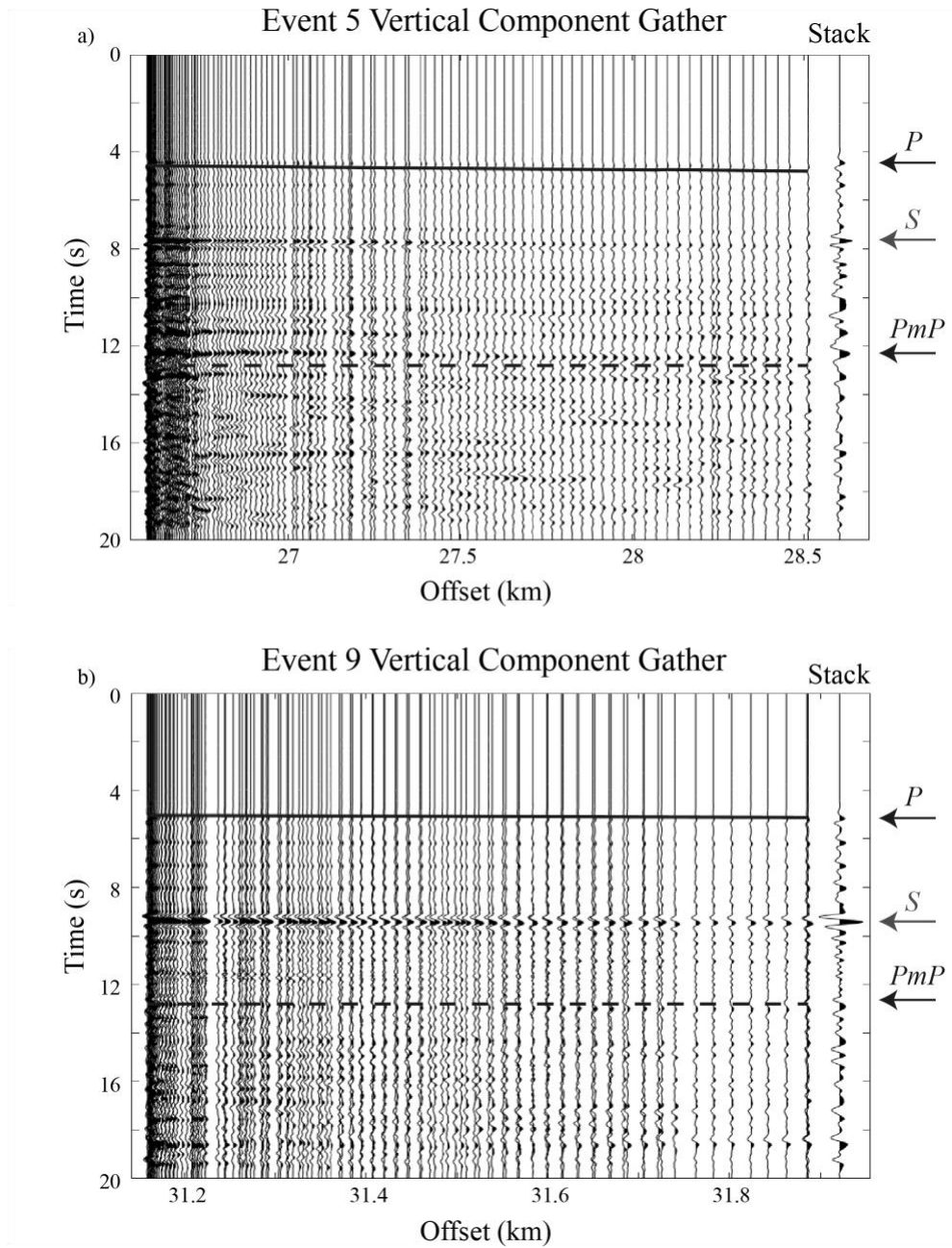


Figure 4. a) A single-event receiver gather of the vertical components recorded by the east-west linear array nodal stations for event 5 in the supplementary material. Each trace is low-pass filtered to 2 Hz and gained by a power of t to approximately equalize the amplitude decay with time. The solid and dashed lines are the predicted arrival times for the P and PmP from ray tracing after a

move-out correction for the PmP arrival. The rightmost trace is the event stack. The arrows on the right denotes the observed arrival-times of the P , S , and PmP on the stacked trace. b) is a similar plot for event 9.

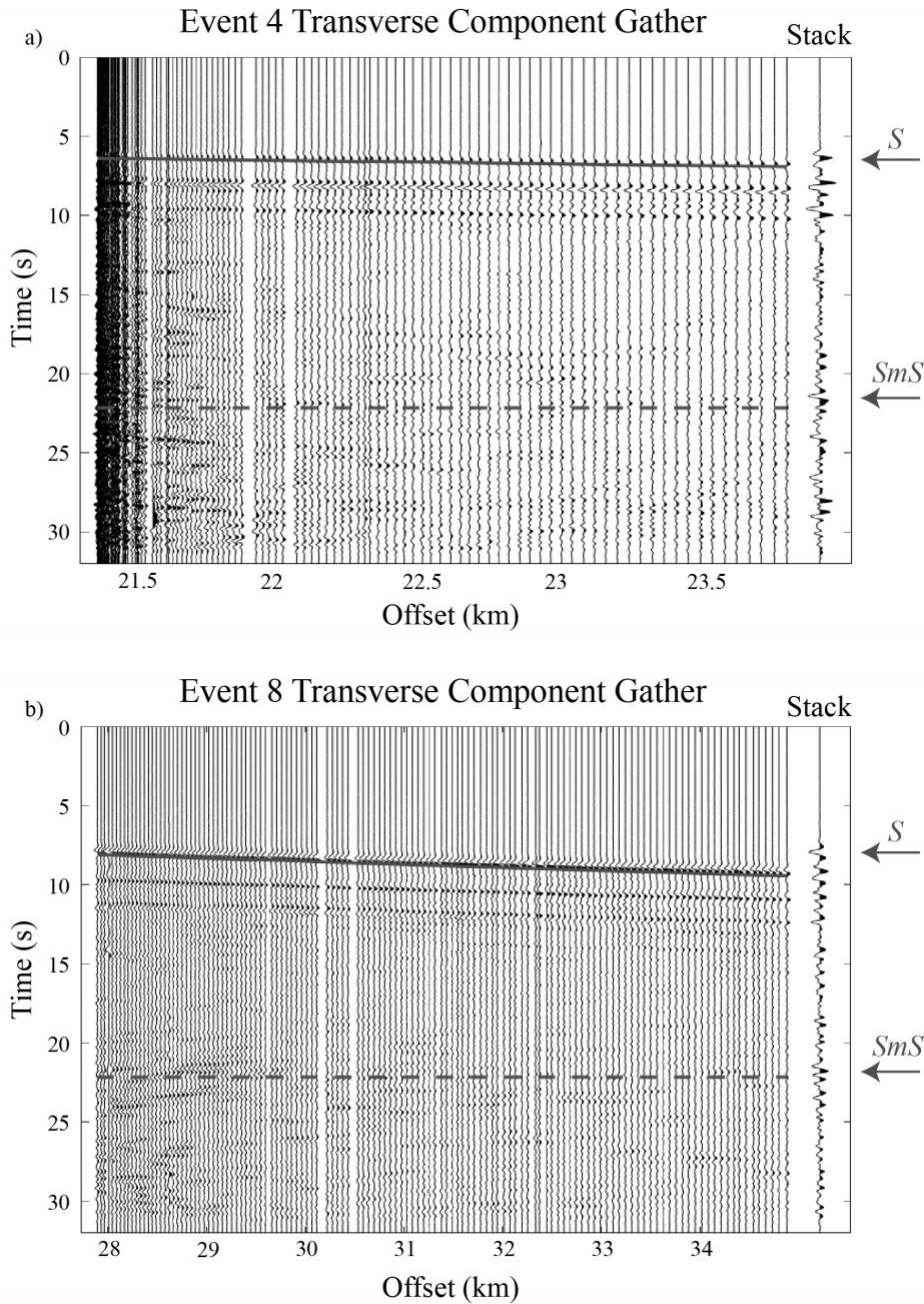


Figure 5. a) A single-event receiver gather of the transverse component recorded by east-west linear array stations for event 4 in the supplementary material. Each trace is low-pass filtered to 1.5 Hz and gained by a power of t to approximately equalize the amplitudes in time. The solid and dashed lines are the predicted S and SmS arrivals after a move-out correction for the SmS arrival-time. The rightmost trace in each single-event receiver gather is the stack. b) is a similar plot for

event 8.

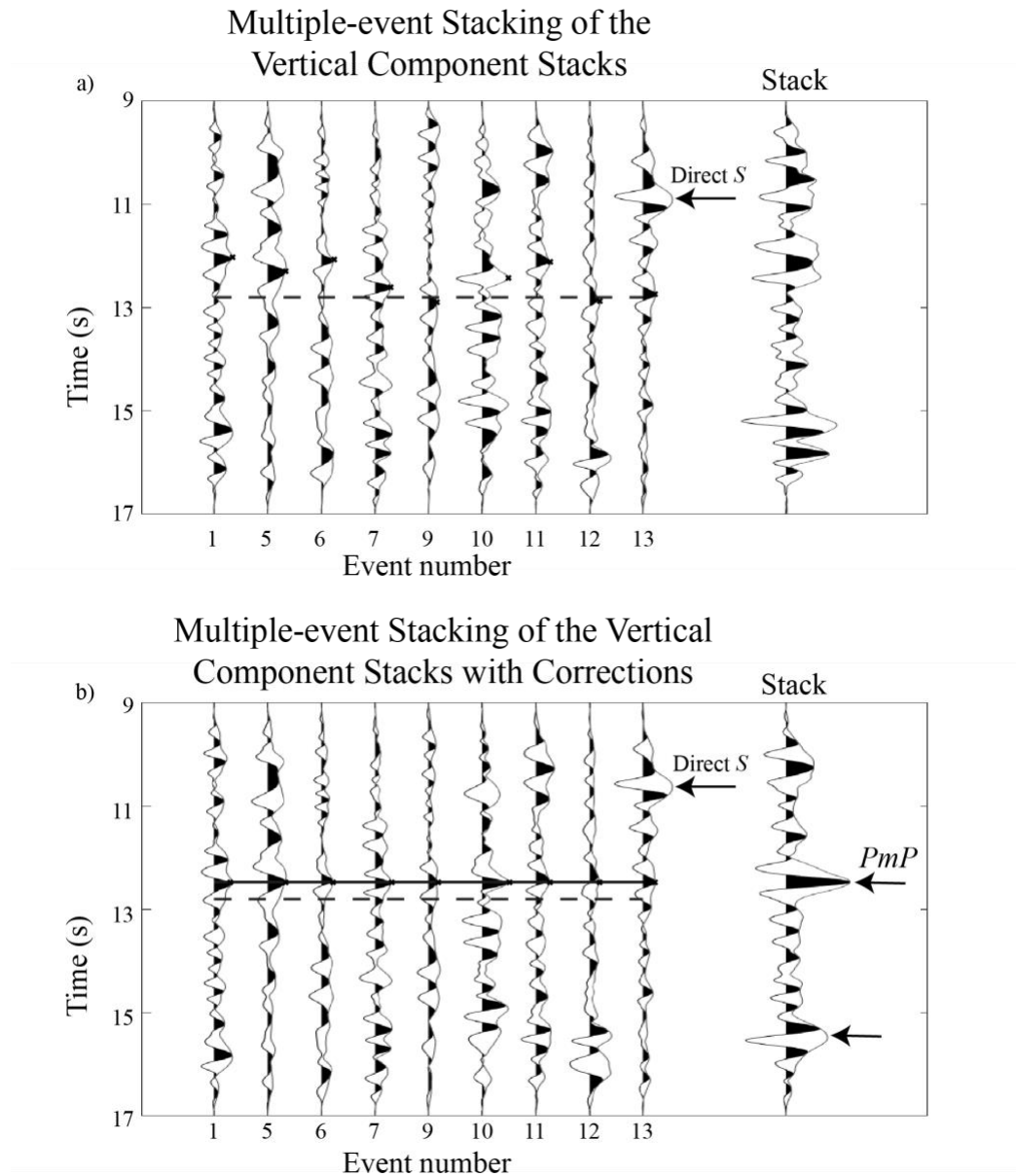


Figure 6. a) shows the multiple-event stacking of the vertical component stacks. Each trace on the left is a single-event receiver stack result. The rightmost trace is the multiple-event stacked trace. For each trace the envelope is also shown. The dashed line is the predicted time of the normal moveout corrected predicted PmP arrivals for the OGS model. The direct S is also shown for one

event. b) shows the multiple-event stack of the vertical component after static and polarity corrections. The dashed line is the predicted moveout corrected time of the PmP from the OGS model. The solid line is the average of the envelope peaks denoting the predicted Moho reflection time. The direct S wave is shown by arrows in both a) and b). Static corrections and polarity corrections are applied to the individual traces prior to stacking, with the stack shown on the right. The inferred PmP arrival is shown by an arrow. The lower arrow on the stack could be the location of the surface reflected $sPmP$ arrival.

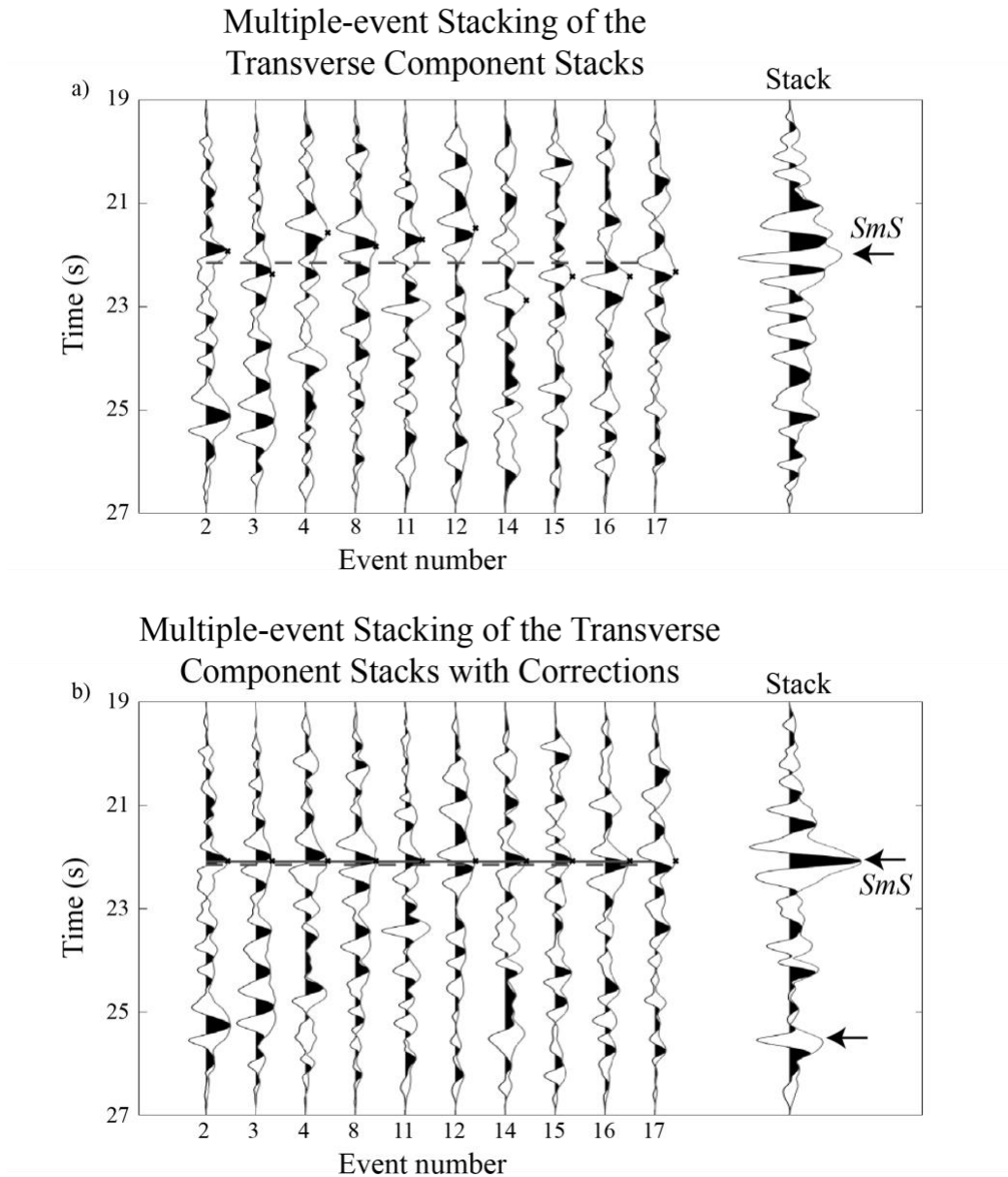


Figure 7. a) shows the multiple-event stacking of the transverse component stacks. Each trace on the left is a single-event receiver stack result. The dashed line is the predicted time for the moveout corrected SmS from the OGS model. The rightmost trace is the multiple-event stacked trace. b) shows the multiple-event stack of the transverse component after static and polarity corrections. The dashed line is the predicted time for the moveout corrected SmS from the OGS model. The solid line is the average of the envelope peaks denoting the inferred Moho reflection time. Static corrections and polarity corrections are applied to the individual traces prior to stacking, with the

stack shown on the right. The inferred SmS arrival is shown by an arrow. The lower arrow on the stack could be the location of the surface reflected $sSmS$ arrival.

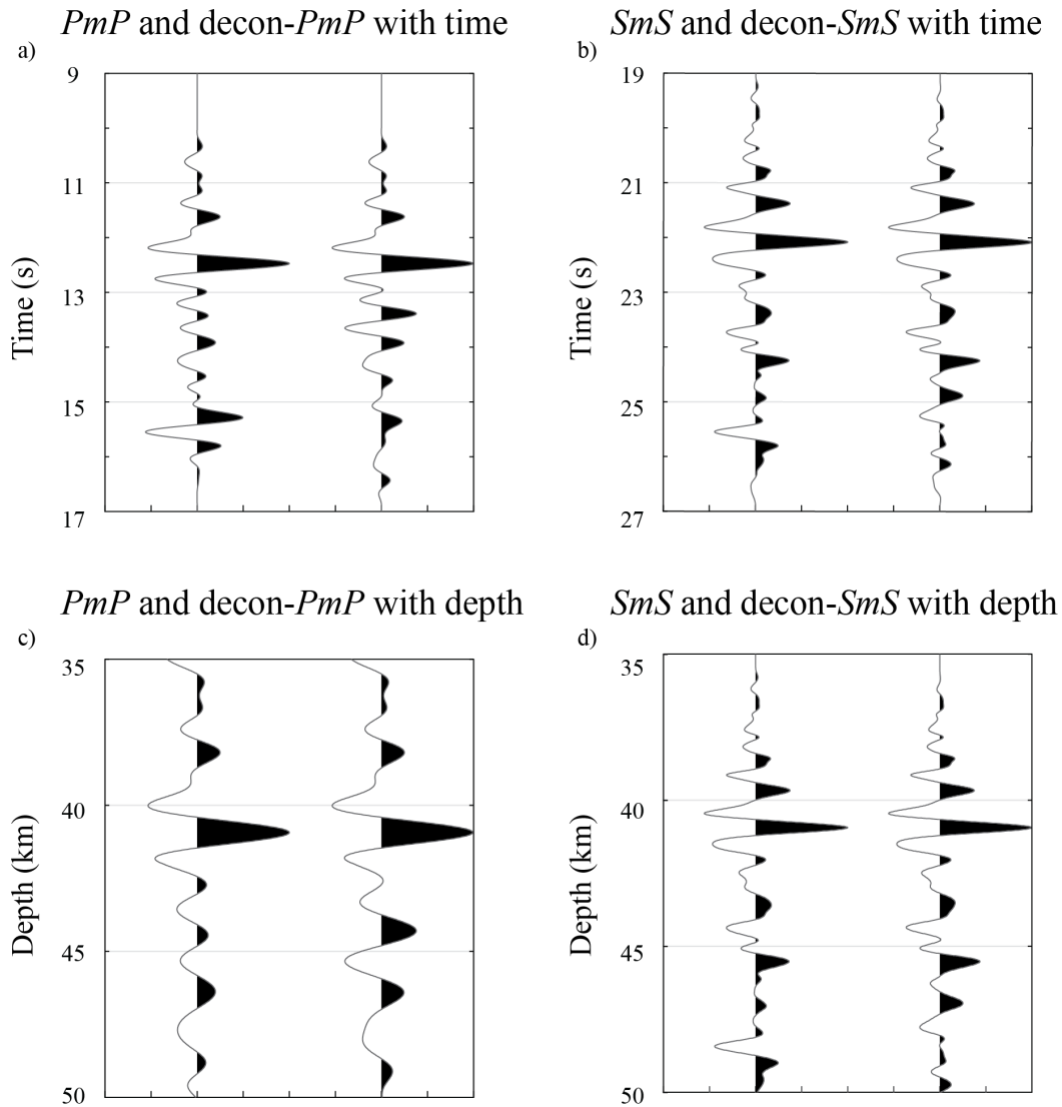


Figure 8. a) shows the PmP and decon- PmP traces with time. The left trace is the multiple-event stack of the vertical component after static and polarity corrections. A tapering is applied between 9 to 11 seconds to mitigate the effect of direct S arrivals. Slight filtering is also applied to make the frequency content on the vertical component comparable to that of the transverse component. The right trace is the deconvolution of the left trace to remove the later pulse between 15 to 16 seconds. b) shows the SmS and decon- SmS traces with time. The left trace is the multiple-event stack of the transverse component after static and polarity corrections. The right trace is the deconvolution of the left trace to remove the later pulse between 25 to 26 seconds. c) shows the PmP and decon- PmP traces with depth. The OGS P -wave velocity model is used to perform the

time to depth conversion. The Moho depth obtained for the P -wave Moho reflection is at 41 km. d) shows the SmS and decon- SmS traces with depth. The S -wave velocity calculated from OGS P -wave velocity using a 1.77 V_p/V_s ratio is used to perform the time to depth conversion. The Moho depth obtained from the S -wave Moho reflection is also at 41 km consistent with the estimate from the PmP traces with depth.

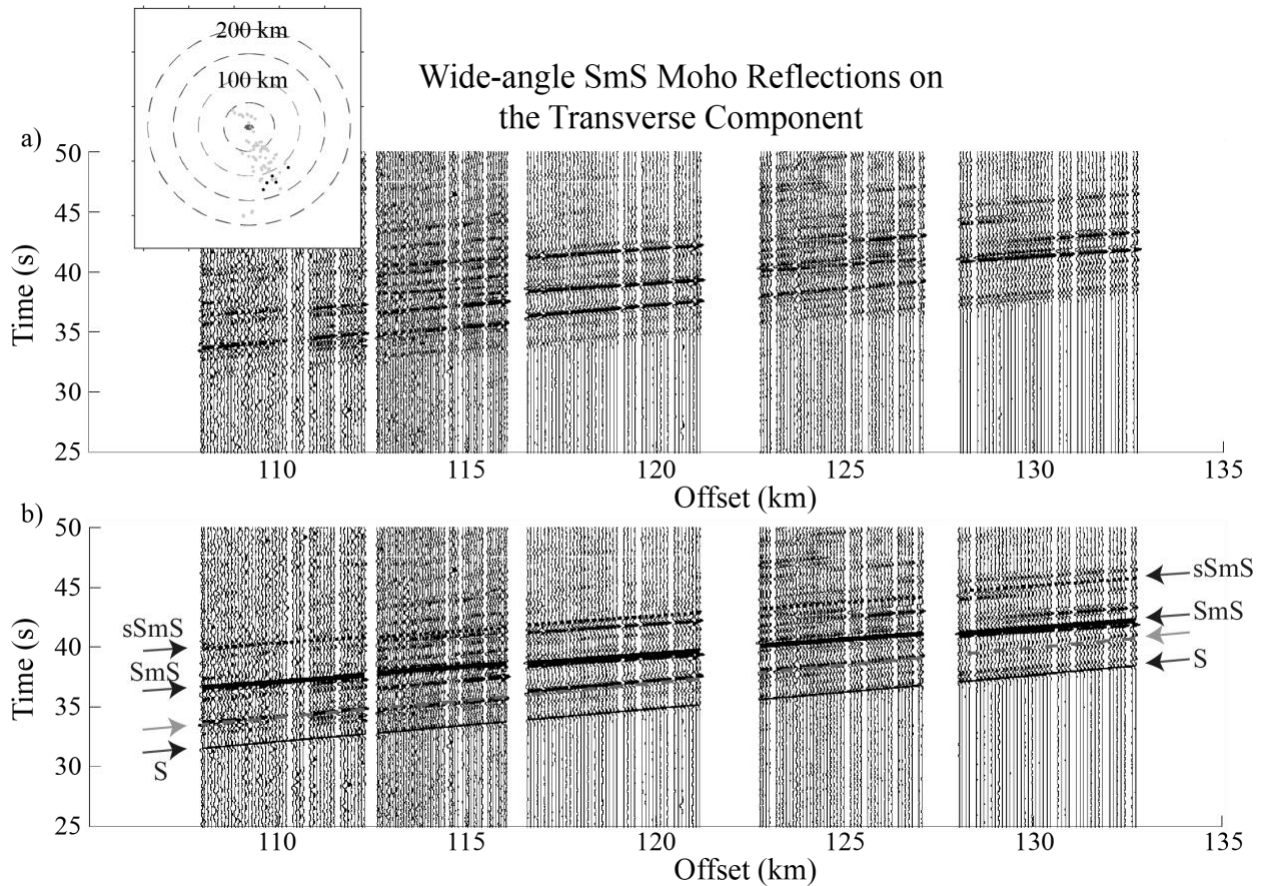


Figure 9. a) Composite record section of the wide-angle SmS Moho reflections on the transverse component, recorded on the left north-south linear nodal array stations. Each trace is low-pass filtered to 1.5 Hz. The inset map shows the location of earthquakes, denoted by gray dots. The black dots are selected for the plot. b) shows the composite record section with identified phase shown. The thick solid line and arrows show the predicted SmS arrival. The arrival-times are ray traced from the modified OGS model with a V_p/V_s of 1.77 and the depths in the OGS seismic catalog. The thin solid line and arrows show the direct S arrival. The surface reflected Moho reflection phase $sSmS$ is also denoted by the dotted line and arrows. The light gray dashed line and arrow show either a surface reflected direct wave sS or a surface wave with a 3.45 km/s apparent velocity in a narrow frequency band.

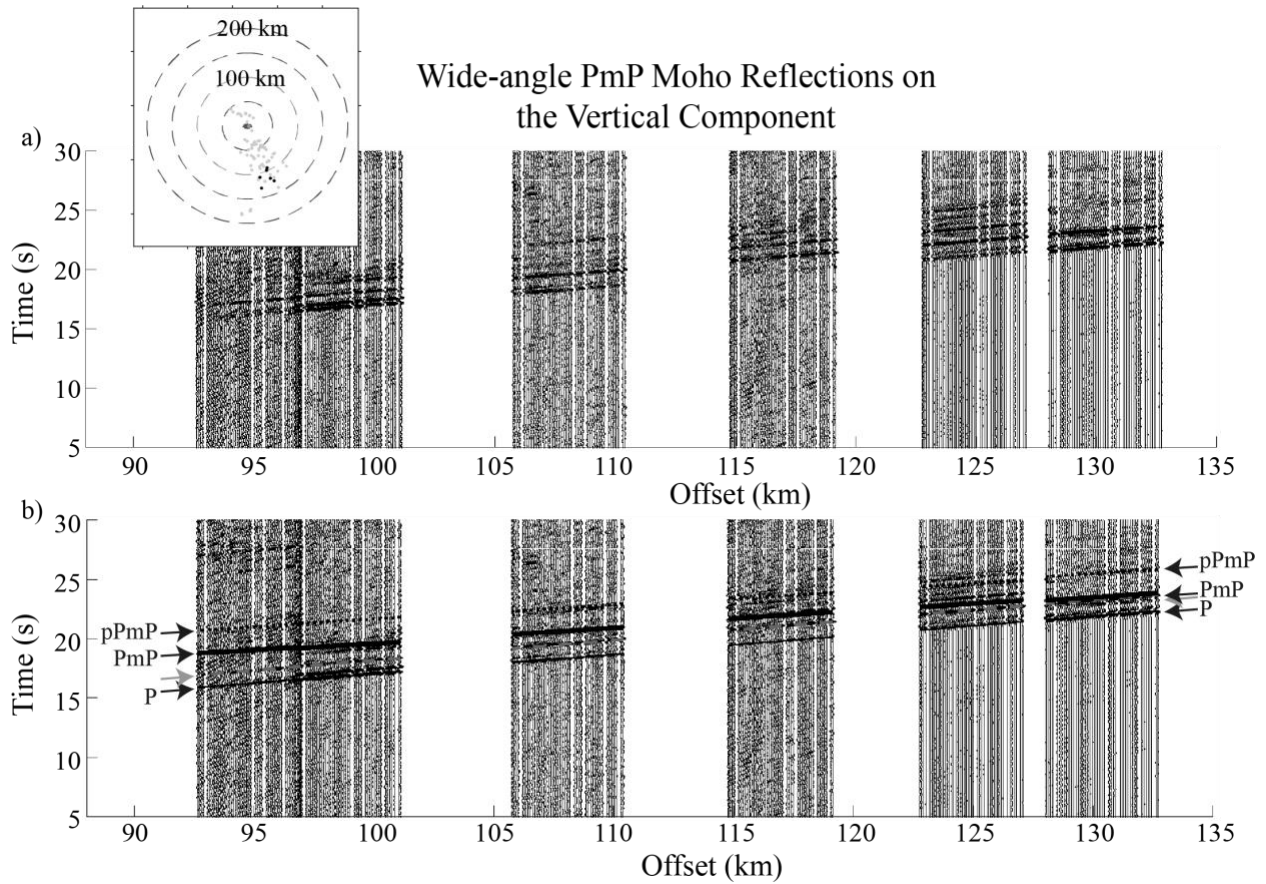


Figure 10. a) Composite record section of the wide-angle PmP Moho reflections on the vertical component, recorded on the left north-south linear nodal array stations. Each trace is low-pass filtered to 2 Hz. The inset map shows the location of earthquakes, denoted by gray dots. The black dots are selected for the analysis. b) shows the composite record section with identified phase shown. The thick solid line and arrows show the predicted PmP arrival. The arrival-times are ray traced from the modified OGS velocity model and the depth in the OGS seismic catalog. The thin solid line and arrows show the direct P arrival. The surface reflected Moho reflection phase $pPmP$ is also denoted by the dotted line and arrows. The light gray dashed line and arrows show a possible surface reflected direct wave pP .